

High-pressure, temperature elasticity of Fe- and Al-bearing MgSiO₃: implications for the Earth's lower mantle

Shuai Zhang^{a,*}, Sanne Cottaar^b, Tao Liu^c, Stephen Stackhouse^c, Burkhard Militzer^{a,d}

^a*Department of Earth and Planetary Science,*

University of California, Berkeley, California 94720, USA

^b*Department of Earth Sciences, University of Cambridge, Cambridge, UK*

^c*School of Earth and Environment, University of Leeds, Leeds LS2 9JT, UK*

^d*Department of Astronomy, University of California, Berkeley, California 94720, USA*

Abstract

Fe and Al are two of the most important rock-forming elements other than Mg, Si, and O. Their presence in the lower mantle's most abundant minerals, MgSiO₃ bridgmanite, MgSiO₃ post-perovskite and MgO periclase, alters their elastic properties. However, knowledge on the thermoelasticity of Fe- and Al-bearing MgSiO₃ bridgmanite, and post-perovskite is scarce. In this study, we perform *ab initio* molecular dynamics to calculate the elastic and seismic properties of pure, Fe³⁺- and Fe²⁺-, and Al³⁺-bearing MgSiO₃ perovskite and post-perovskite, over a wide range of pressures, temperatures, and Fe/Al compositions. Our results show that a mineral assemblage resembling pyrolite fits a 1D seismological model well, down to, at least, a few hundred kilometers above the core-mantle boundary, i.e. the top of the D'' region. In D'', a similar composition is still an excellent fit to the average velocities and fairly approximate to the density. We also implement polycrystal plasticity with a geodynamic model to predict resulting seismic anisotropy, and find post-perovskite with predominant (001) slip across all compositions agrees best with seismic observations in the D''.

Keywords: lower mantle; pyrolite; bridgmanite; post-perovskite; elastic properties; first principles

* Corresponding author.

E-mail address: shuai.zhang01@berkeley.edu (S. Zhang)

1. Introduction

Fe-bearing perovskite (Pv, a.k.a. bridgmanite) and post-perovskite (pPv) are the most abundant minerals in the Earth's lower mantle. A good knowledge of their elastic properties under relevant high-pressure (P) and temperature (T) conditions is of fundamental importance for understanding the structure and dynamics of the Earth's interior. Experiments have suggested that Pv hosts ~ 10 mol.% iron and a slightly lower amount of Al in the pyrolitic model composition, expected from the top to, at least, the mid-lower mantle (Irifune et al., 2010). It has also been known that the amount of Fe in different ionic states can be controlled by oxidation, charge disproportionation and the existence of Al (Xu et al., 2015). Despite of this, it is still debated how much iron remains in Pv, how it is distributed between Pv and pPv, and whether Fe^{2+} disproportionates to form $\text{Fe}^{3+} + \text{Fe}^0$ metal, or partitions into magnesiowüstite or melt, in the lowermost mantle (e.g., Mao et al., 2004; Irifune et al., 2010). Currently, there is scarce experimental data available on the elastic properties of these systems (Murakami et al., 2012), and the uncertainty could be huge, due to the interplay between the above factors and technical issues relating to the extreme conditions. This necessitates theoretical methods, which are not limited by the same constraints as experiments and have been proven to be a powerful tool in determining the elastic properties of minerals at lower mantle conditions.

There have been several reports on the elastic properties of these Pv and pPv systems using first-principle calculations. However, these have mainly focused on pure MgSiO_3 for high-T conditions (Oganov et al., 2001; Wentzcovitch et al., 2004, 2006; Stackhouse et al., 2005; Stackhouse and Brodholt, 2007; Zhang et al., 2013), or Fe/Al-bearing systems at 0 K (Kiefer et al., 2002; Caracas and Cohen, 2005; Li et al., 2005a; Stackhouse et al., 2005,

2006, 2007; Tsuchiya and Tsuchiya, 2006), because of the high computational cost and the complex structural and electronic properties of Fe/Al-bearing systems at high P and T .

Examples on this complexity include the pressure-induced high-spin (HS) to low-spin (LS) transition in iron (Badro et al., 2004) and challenges arising from the large number of mechanisms that iron can enter the Pv and pPv structures. Ferrous iron substitutes for Mg in the pseudo-dodecahedral A (Mg-) site, but for ferric iron charge balance requires the coupled substitution of Fe-Al or Fe-Fe pairs (Zhang and Oganov, 2006a), with one cation at the A site and the other at the octahedral B (Si-) site. Incorporation of ferric iron via the oxygen vacancy mechanism is not expected in Pv and pPv at lower mantle conditions (Brodholt, 2000).

Ferrous iron, in the A site, is expected to remain in the HS state, in Pv and pPv, at all mantle conditions (Hsu et al., 2011a; Yu et al., 2012). In contrast, ferric iron undergoes a spin transition at lower-mantle pressures, as the crystal field splitting surpasses the spin pairing energy, which breaks the Hund's rule that predicts all five d electrons in Fe^{3+} have the same spin (HS state) and stabilizes the LS state (3 electrons spin up, 2 down). The spin transition of ferric iron is expected to start at about 75 GPa at the A site, and at much lower pressures at the B site (Zhang and Oganov, 2006b; Li et al., 2005b; Hsu et al., 2011b, 2012).

In recent years, there have been several studies on the effects of ferrous and ferric iron on the thermoelastic properties of Pv and pPv (Metsue and Tsuchiya, 2011; Tsuchiya and Wang, 2013; Shukla et al., 2015). To date, agreement with seismological models of the lower mantle has not been reached. One potential reason is that the influence of Al^{3+} has not yet been included, and another could be related to the possible inadequacy of using the quasi-harmonic approximation (QHA) in computing thermoelasticity at high- P and T . There has been one study that used density functional molecular dynamics (DFT-MD) to

calculate the properties of Pv and pPv enriched with ferrous iron (Muir and Brodholt, 2015), but this only reports values at one pressure.

In this letter, we apply DFT-MD to determine the elastic properties of ferrous and ferric iron-bearing Pv and pPv over a wide range of pressure and temperature conditions relevant to the Earth's lower mantle. In the case of ferric iron, Fe-Al and Fe-Fe substitution are considered. DFT-MD naturally accounts the anharmonicity of lattice dynamics, which is important for describing the elastic behavior of minerals at high T (above the Debye temperature) and has been used in several previous studies (Stackhouse et al., 2005; Zhang et al., 2013). In the case of ferrous iron only the HS state is considered, whereas for ferric iron different Fe-Fe or Fe-Al compositions in various possible spin states are considered. The structures are included in the supplementary material. High- T lattice parameters are obtained by performing DFT-MD simulations at constant pressures (NPT ensemble), which is followed by fixed-cell (NVT) calculations on strained structures to calculate the elastic coefficients and other elastic properties. Based on these calculations, we derive the seismic properties of a mineral assemblage to compare with a 1D seismological model, with the aim of constraining the mineral composition of the lower mantle. We further exemplify shear wave anisotropic properties resulting from deformation within a deep subducting slab and discuss the implications for seismic observations of shear wave anisotropy.

2. Theory

2.1. Computational methods

Our calculations are performed using the Vienna *ab initio* simulation package (VASP) (Kress and Furthmüller, 1996). The local density approximation (LDA)-based (Ceperley and Alder, 1980) exchange-correlation functional is used. It has been shown that in some cases, standard DFT functionals can fail to predict the correct electronic properties of iron-

bearing minerals, and inclusion of a Hubbard U term leads to improved predictions of their electronic, structural and elastic properties (Stackhouse et al., 2010). However, a recent study suggests that provided standard DFT functionals produce the correct insulating ground states and correct orbital occupancy, the structural and elastic properties predicted with them should be similar to those with a U term (Hsu et al., 2011a). We confirmed this conclusion by comparing the results of calculations with and without a U term, for a select number of iron-bearing Pv structures (Table S4, supplementary material), and performed the remainder without a U term.

The supercell sizes $2 \times 2 \times 1$ (80-atom) for Pv, and $3 \times 1 \times 1$ (60-atom) or $4 \times 1 \times 1$ (80-atom) for pPv are used. We employ projector augmented wave pseudopotentials with core radii equaling 2.2, 1.9, 2.0, 1.9, and 1.52 Bohr for Fe, Al, Mg, Si, and O, respectively. In static calculations, the plane wave energy cutoff is set to 800 eV, and k -mesh of $2 \times 2 \times 4$ (for Pv supercell) or $6 \times 6 \times 6$ (for pPv supercell) are chosen for Brillouin zone sampling. The enthalpy is evaluated based on structures that are all relaxed until all forces are smaller than 10^{-4} eV/Å. In MD simulations, we follow previous studies (Stackhouse and Brodholt, 2007; Zhang et al., 2013) and use time step of 1 fs, energy cutoff of 500 eV and only the Γ point to sample the Brillouin zone. Tests show that using these settings the elastic properties are converged to within statistical error. We use the Nosé thermostat to control the temperature (Nosé, 1984). The lattice constants are obtained by averaging over NPT trajectories. These are then used in the NVT simulations. For calculating the elastic constants from linear stress-strain relations, three axial and one triclinic strain are applied to the cell. During NPT, we fix the cell to be orthorhombic to avoid unnecessary fluctuations. The same averaging scheme is applied to NVT trajectories to retrieve stress components and energies. The NPT and NVT trajectories are typically over 3 ps and 5 ps, respectively. The convergence is shown in the supplementary material.

For ferrous iron we include four Fe^{2+} in 80-atom unit cells of Pv and pPv to construct $(\text{Mg}_{1-x}\text{Fe}_x)\text{SiO}_3$ structures with an atomic percent x equal to 25%. For ferric iron we include one or two $\text{Fe}^{3+}\text{-M}^{3+}$ (M representing Fe or Al) pairs in MgSiO_3 by charge-coupled substitution $\text{Fe}_{\text{Mg}}\text{M}_{\text{Si}}$ in order to construct $(\text{Mg}_{1-x}\text{Fe}_x)(\text{Si}_{1-x}\text{M}_x)\text{O}_3$ structures with atomic percent x equal to 6.25% or 12.5% for Pv, and 8.33% or 16.7% for pPv. Such iron or aluminum compositions are relevant to the lower mantle (Irifune et al., 2010). For Fe^{2+} in these models, we consider only the HS (spin momentum $S=4/2$) ferromagnetic state, whereas for Fe^{3+} we consider both the HS ($S=5/2$) and LS ($S=1/2$) states. Intermediate-spin states are not considered because they have been found to be energetically disfavored in previous studies (Hsu et al., 2011b). For systems with multiple ferric iron cations, we take into account all possible spin configurations, including pure HS, pure LS, or HS-LS mixtures in the ferromagnetic (FM) or antiferromagnetic (AFM) states. Our results confirm conclusions reached in several previous DFT calculations on the site-dependence and values of the transition pressure, i.e., Fe^{3+} has higher transition pressure at the A-site than at B-site. This enables us to disregard unlikely configurations, for example, B-site Fe^{3+} in HS at 100 GPa. In spite of this, there are still an ample amount of configurations to consider.

For ferric iron-bearing structures, we first perform a structural relaxation at 0 K by fixing the spin state of each iron in the system. For the different compositions, we compare the enthalpies of the different spin states at each pressure, in order to determine the most stable configurations. The magnetic entropy is the same for Fe^{3+} at either A or B site whether it is HS or LS ($S_{\text{mag}} = k_B \ln 6$, see supplementary material). If we assume the vibrational entropy of the different spin configurations to be similar, then the enthalpies provide a good approximation to the most stable spin states at high temperature without having to calculate the Gibbs free energy. We limit our studies of high temperature elasticity mainly to the most stable configurations at 0 K. In spite of this, because there

does not exist a perfect way of describing the correlation effects of 3d electrons of iron and temperature could potentially stabilize the HS state, at high temperature we selectively carry out additional calculations on configurations other than the most stable ones at 0 K, in order to get a more complete picture on the effect of different magnetic states on the elastic properties.

2.2. Calculation of elastic, seismic, and thermodynamic properties

The elastic constants are determined assuming the linear stress-strain relation $\sigma_\alpha \propto C_{\alpha\beta} \epsilon_\beta$, although higher-order terms become more significant for larger strains (Zhang et al., 2013 and supplementary material). In our calculations, we choose an optimized strain of magnitude $\epsilon = \pm 0.5\%$ (Militzer et al., 2011). The orthorhombic symmetry of Pv and pPv allow us to obtain the nine independent elastic constants by applying three axial strains and one triclinic strain (Stackhouse and Brodholt, 2007). The polycrystalline bulk and shear moduli, K and G , are determined consequently using the Voigt averaging scheme. A comparison with the Voigt-Reuss-Hill (VRH) scheme is shown in the supplementary Table S5.

The direction-dependence of the phase velocities is governed by the Christoffel equation $[\rho v^2 \delta_{ik} - C_{ijkl} n_j n_l][u_k] = 0$, where C_{ijkl} is the elastic tensor where the indexes ij and kl correspond to the above α and β via the Voigt notation: $\{11; 22; 33; 23; 13; 12\} \rightarrow \{1; 2; 3; 4; 5; 6\}$, δ_{ik} is the Kronecker delta and $\{n_j\}$ denotes the wave propagation direction. The solution to the Christoffel equation yields three eigenvalues that are the phase velocities of the three wave modes, P, SV and SH, that can exist in an anisotropic solid. Because of the high velocity, the transmission of seismic waves in the lower mantle is primarily an adiabatic process rather than an isothermal one. Therefore, we add an adiabatic correction according to (Wallace, 1972)

$$C_{\alpha\beta}^S = C_{\alpha\beta}^T + \frac{TV}{c_\eta} b_\alpha b_\beta, \quad (1)$$

where $b_\alpha = \left(\frac{\partial\sigma_\alpha}{\partial T}\right)_\eta$, C_η is fixed-configuration heat capacity approximated by $C_V = \left(\frac{\partial E}{\partial T}\right)_V$, which can be obtained by two additional simulations for each structure with fixed volume and temperatures changed by ± 100 K.

In order to compare the results with experimental data, one has to apply a pressure correction, because of the well-known fact that LDA underestimates lattice constants and thus the pressure. One simple way is to calculate at experimentally determined ambient-pressure volume in the static condition, and then apply the pressure difference as a constant shift (Oganov et al., 2001) ΔP to all computed pressures regardless of P , T , Fe/Al compositions and the mineral phases. It is worthwhile to note that this is by no means a perfect solution, but works reasonably well (Stackhouse and Brodholt, 2007; Militzer et al., 2011; Zhang et al., 2013). With a careful estimation on the ambient-pressure volume in the static condition (see supplementary material), we determined $\Delta P = 4.0 \pm 0.8$ GPa.

3. Results and discussion

3.1. Spin states

The most stable spin configurations at 0 K for the ferric iron systems are summarized in Table 1. In $(\text{Mg}_{1-x}\text{Fe}_x)(\text{Si}_{1-x}\text{Fe}_x)\text{O}_3$ Pv, Fe^{3+} at the A-site undergoes a spin transition below 50 GPa; with Al^{3+} in the B-site, the transition pressure P_{tr} increases to over 50 GPa. In both cases P_{tr} of A-site Fe^{3+} increases with x . B-site Fe^{3+} is always LS. The dependence of P_{tr} on x reflects the importance of the Fe-M (M=Fe or Al) interactions. In pPv, Fe^{3+} in the A-site is always LS above 100 GPa, except for $(\text{Mg}_{1-x}\text{Fe}_x)(\text{Si}_{1-x}\text{Al}_x)\text{O}_3$ with $x=17\%$, where two pairs of A-B sites are occupied by one Fe^{3+} - Fe^{3+} and one Al^{3+} - Al^{3+} pair, where the Fe^{3+} at the A-site is always HS. B-site Fe^{3+} is always LS, as found for Pv.

Table 1
The stable spin configurations, denoted by the spin state of Fe³⁺ at the A site (or A site - B site), of Fe³⁺-Fe³⁺ and Fe³⁺-Al³⁺ bearing Pv and pPv at $T = 0$ K and different pressures. No pressure correction is applied.

P[GPa]	Iron spin state				
	<i>Pv</i>	(Mg _{1-x} Fe _x)(Si _{1-x} Fe _x)O ₃		(Mg _{1-x} Fe _x)(Si _{1-x} Al _x)O ₃	
		x=6.25%	x=12.5%	x=6.25%	x=12.5%
25		HS-LS, fm	HS-LS, fm	HS	⁽¹⁾ HS-HS, afm
50		LS-LS, afm	HS-LS, fm	HS	⁽¹⁾ HS-HS, afm
75		LS-LS, afm	LS-LS, afm	LS	⁽²⁾ HS-LS, fm
100		LS-LS, afm	LS-LS, afm	LS	⁽²⁾ LS-LS, afm
125		LS-LS, afm	LS-LS, afm	LS	⁽²⁾ LS-LS, afm
	<i>pPv</i>				
		x=8.3%	x=16.7%	x=8.3%	x=16.7%
100		LS-LS, fm	LS-LS, fm	LS	⁽²⁾ HS-LS, fm
125		LS-LS, fm	LS-LS, fm	LS	⁽²⁾ HS-LS, fm
150		LS-LS, fm	LS-LS, fm	LS	⁽²⁾ HS-LS, fm

(1) two Fe-Al pairs, spin configuration denoted by Fe³⁺ at pair1-pair2; (2) one Fe-Fe and one Al-Al pair.

Comparing with previous studies (e.g., Zhang and Oganov, 2006b; Li et al., 2005b; Caracas, 2010; Hsu et al., 2011b; Hsu et al., 2012; Yu et al. 2012; Catalli et al., 2011; Fujino et al., 2014), the transition pressures found here are generally lower. This can be understood from the following aspects: 1) LDA typically underestimate the lattice constants and thus the pressure; 2) on-site Coulomb repulsion (Hubbard U) increases the transition pressure for both A and B sites; 3) the configurations (structures files in this study are included as supplementary material) may vary in different calculations; 4) the distortions of crystallographic sites are different between one-site and two-site substitution by Fe³⁺ or Al³⁺.

We also note that predicting spin states is very complicated and involves many issues that are not understood. For example, it is debated whether Fe³⁺ can occupy both A- and B-sites or exclusively the A-site, and if there is exchange from the A- to the B-site. However, because spin state has only a minor effect on elastic properties (Stackhouse et al., 2007; Li et al., 2005b and Table 2), this will have little influence on our calculated seismic

properties. For example, for all compositions tested (Table 2), the difference between the seismic properties of the high and low-spin states is on average 0.5%, with a maximum of 1%.

Table 2
Comparison on density, adiabatic bulk modulus K^S , shear modulus G , and bulk, shear, and compressional velocities V_b , V_s , and V_p at different spin states. The notation for spin states is the same as in Table 1. Numbers in parenthesis denote the error of the corresponding values.

	ρ [kg/m ³]	K^S [GPa]	G [GPa]	V_b [km/s]	V_s [km/s]	V_p [km/s]
Pv (Mg _{1-x} Fe _x)(Si _{1-x} Fe _x)O ₃ $x=12.5\%$ 75 GPa, 1500 K						
HS-LS	5279	513.22(3.82)	225.13(2.76)	9.86(0.04)	6.53(0.04)	12.41(0.04)
LS-LS	5301	514.38(8.23)	228.55(5.24)	9.85(0.08)	6.57(0.08)	12.43(0.08)
Pv (Mg _{1-x} Fe _x)(Si _{1-x} Al _x)O ₃ $x=12.5\%$ 125 GPa, 1500 K						
⁽¹⁾ HS-HS	5607	674.69(4.46)	294.55(3.78)	10.97(0.04)	7.25(0.05)	13.80(0.04)
⁽²⁾ LS-LS	5614	681.87(4.25)	294.10(3.48)	11.02(0.03)	7.24(0.04)	13.83(0.04)
pPv (Mg _{1-x} Fe _x)(Si _{1-x} Fe _x)O ₃ $x=8.33\%$ 100GPa, 1500 K						
HS-LS	5512	600.21(4.40)	293.77(3.76)	10.43(0.04)	7.30(0.05)	13.41(0.05)
LS-LS	5519	587.15(5.60)	299.88(6.07)	10.31(0.05)	7.37(0.07)	13.37(0.07)
pPv (Mg _{1-x} Fe _x)(Si _{1-x} Al _x)O ₃ $x=16.67\%$ 150 GPa, 2500 K						
⁽²⁾ HS-HS	5879	745.25(8.77)	335.59(7.93)	11.26(0.07)	7.56(0.09)	14.24(0.08)
⁽²⁾ HS-LS	5881	758.91(7.62)	340.14(7.53)	11.36(0.06)	7.61(0.08)	14.36(0.07)
⁽²⁾ LS-LS	5889	761.04(8.07)	336.40(8.56)	11.37(0.06)	7.56(0.10)	14.33(0.08)

(1) two Fe-Al pairs, spin configuration denoted by Fe³⁺ at pair1-pair2; (2) one Fe-Fe and one Al-Al pair.

3.2. Pv→pPv phase transition

By comparing enthalpies, we determine the Pv→pPv transition pressure (Table 3). For pure MgSiO₃, our finding is in agreement with previous DFT-LDA calculations (83.7-100 GPa, according to Oganov and Ono, 2004 and Tsuchiya et al., 2004) as well as experiments (91-116 GPa, extrapolated to $T = 0$ K based on Fig. 4 in Shim, 2008). The transition pressure decreases with Fe²⁺ or Fe³⁺-Fe³⁺ content (less so in the former case), while it slightly increases and then decreases with the amount of Fe³⁺-Al³⁺. This implies that the existence of Al³⁺ increases the Fe³⁺-bearing Pv→pPv transition pressure, which is consistent with the previously assumed role of Al³⁺ in MgSiO₃ (Zhang and Oganov, 2006a).

Table 3

The Pv→pPv phase transition pressure at $T = 0$ K for pure and Fe²⁺, Fe³⁺-Fe³⁺ or Fe³⁺-Al³⁺ bearing MgSiO₃. The LDA pressure correction $\Delta P = 4.0$ has been applied.

Name	MgSiO ₃	(Mg _{0.75} Fe _{0.25})SiO ₃	(Mg _{1-x} Fe _x)(Si _{1-x} Fe _x)O ₃		(Mg _{1-x} Fe _x)(Si _{1-x} Al _x)O ₃	
			x=8%	x=12.5%	x=8%	x=12.5%
$P_{\text{pv-pPv}}$ [GPa]	94.9	78.8	84.6	71.0	97.2	87.4

3.3. Temperature and pressure dependence of elastic properties

We first compare the elastic constants C_{ij} of MgSiO₃ Pv and pPv from this work with previous calculations (Fig. 1). Our results reconfirm the overall consistency between DFT-MD and QHA and the disagreement at high temperatures, especially for C_{11} , C_{13} , and C_{33} in pPv, as was noted previously (Stackhouse and Brodholt, 2007). More benchmarking comparisons, as well as complete lists on the elastic and seismic properties are given in the supplementary material.

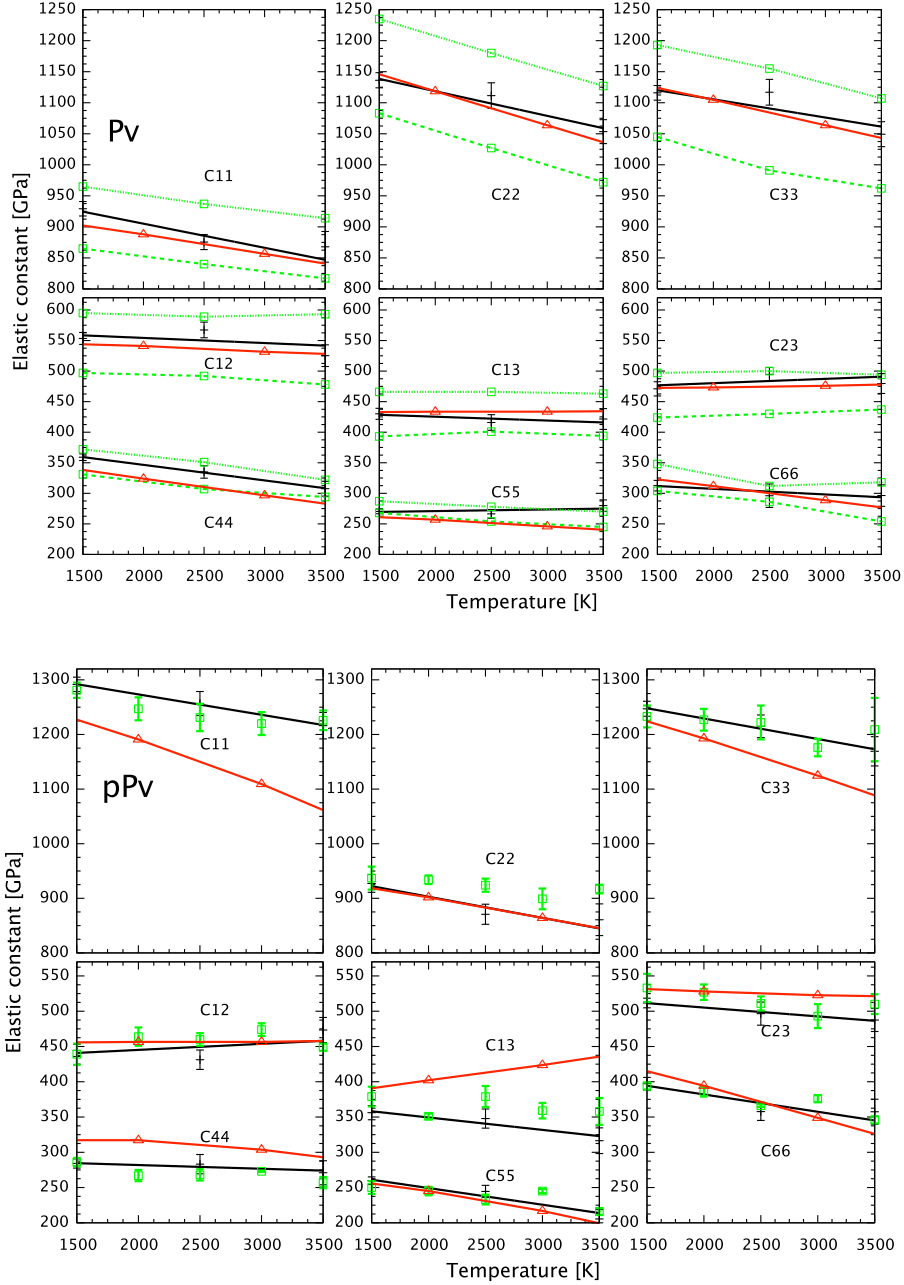


Fig. 1 (color online). The elastic constants of MgSiO_3 Pv (top) and pPv (bottom) at 129 GPa as functions of temperature. Our data are represented with points and fitted with lines in black. Previously DFT-MD studies by Zhang et al. (2013) on Pv at 108 GPa and 137 GPa, shown in green dashed and dotted line squares respectively, and Stackhouse and Brodholt (2007) on pPv at 125 GPa, shown in green squares, and QHA study by Wentzcovitch et al. (2006) on Pv and pPv at 125 GPa, shown in red line triangles, are displayed for comparison.

In order to quantify the effect of T , P , and x on elastic properties, we use the following equation to fit the computed elastic constants and the sound velocities

$$Q(T, P, x) = A_0(x)TP + A_1(x)T + A_2(x)P + A_3(x), \quad (2)$$

where Q is the property being fit, and each parameters $A_i(x)$ is linearly fit to x by $k_i x + b_i$. Data for Pv at 25 GPa are not included to improve the quality of the fitting. Complete lists of the fit parameters can be found in the supplementary material.

Our results show that the elastic constants increase with pressure and mostly decrease with temperature, on the order of 1 for dC_{ij}/dP compared to about 10^{-2} GPa/K for dC_{ij}/dT . C_{12} , C_{13} , and C_{66} remain approximately constant when Fe^{3+} or Al^{3+} contents increases in Pv, while the other six values decrease. In contrast, for pPv, C_{22} , C_{12} and C_{13} increase with the Fe^{3+} or Al^{3+} contents. The effect of Fe^{3+} is akin to that of Al^{3+} and is usually accompanied by slightly higher C_{ij} for Pv but lower C_{ij} for pPv. The magnitude of the compositional derivatives depends on the specific P, T condition.

Analysis of the adiabatic bulk and shear moduli (K^S and G) as a function of P and T , using elastic constants fitted by Eq. (2), shows that G uniformly decreases with x for both Pv and pPv, but K^S does not follow the same trend (Fig. 2). Both moduli are less sensitive to T than to P , similar to the dependence of C_{ij} , and their pressure derivatives are generally less dependent on x at lower T , especially for Pv. The trend for Fe^{2+} is relatively simple---both moduli decrease with temperature, and the pressure derivatives are relatively more stable than the Fe^{3+} -bearing systems. This is understandable considering its more simple substitution mechanism and spin state, and fewer data at varied P and T .

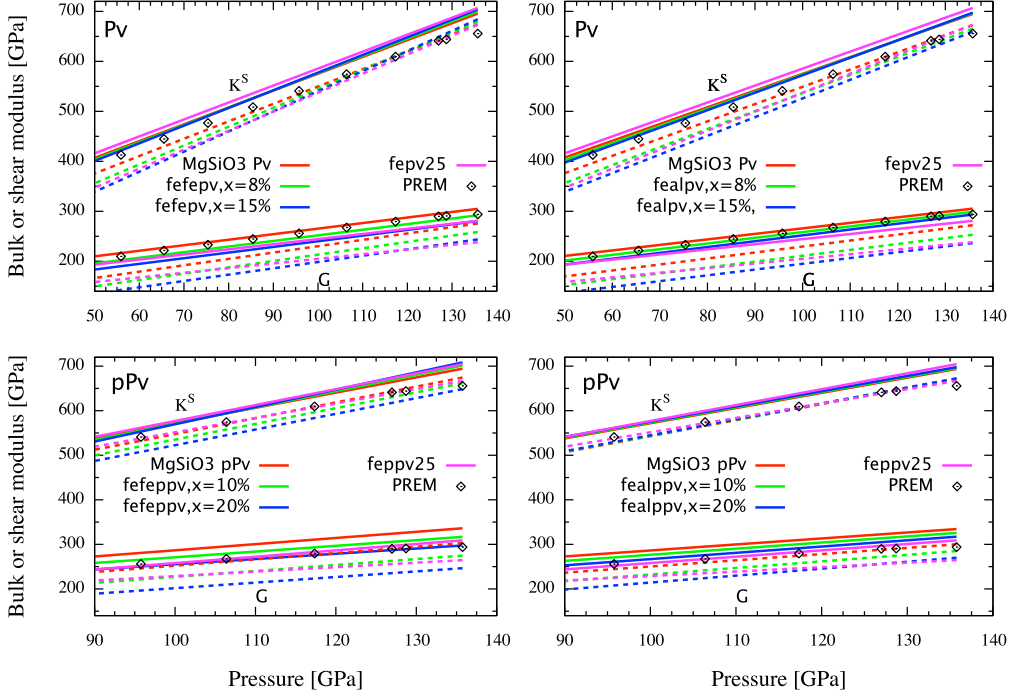


Fig. 2 (color online). Bulk and shear moduli (K^S and G) of pure and Fe^{3+} - Fe^{3+} (fefe, left) or Fe^{3+} - Al^{3+} (feal, right) bearing MgSiO_3 Pv and pPv at 2000 K (solid lines) and 4000 K (dashed lines), in comparison with that of $\text{Mg}_{0.75}\text{Fe}_{0.25}\text{SiO}_3$ (fepv25 and feppv25) and PREM as functions of pressure. Red, green, and blue lines correspond to $x=0$, 8%, and 15% for Pv and 0, 10%, and 20% for pPv, respectively. In each panel, the top lines correspond to K^S , the lower ones correspond to G .

3.4. Temperature, pressure, and composition dependence of sound velocities and density

The compressional (V_p) and shear (V_s) wave velocities are fitted as functions of P , T and x using Eq. (2). The parameters are summarized in Table 4. In this way we can study how the velocities depend on the Fe or Al content x . As is shown in Figs. 3-4, the sound velocities steadily decrease with Fe or Al content, while the effect of Fe is larger, for both Pv and pPv. The pPv phase has higher velocities than Pv. At 110 GPa, the differences in V_p and V_s are 0.7% and 3.2%, respectively; the values further increase to 0.9% and 3.5% when $x=5\%$, and 1.2% and 3.8% when $x=10\%$, for MgSiO_3 with Fe^{3+} and Al^{3+} ; without Al^{3+} , the change in V_s is similar, whereas the change in V_p is less sensitive to x . With Fe^{2+} , the magnitudes of the velocities differences between Pv and pPv are lower but more sensitive

to pressure. At 110 GPa, the velocities of the pPv phase becomes higher than that of the Pv phase by 0.4% and 3.0% for V_p and V_s , respectively.

Table 4
Fit parameters for the sound velocities of ferric iron bearing Pv and pPv. V_p , V_s , and V_b denote the compressional, shear, and bulk velocities, respectively. k and b are in units of km/(GPa.K.s), km/(K.s), km/(GPa.s), and km/s for A_0 , A_1 , A_2 , and A_3 , respectively.

	A_0 -k	A_0 -b	A_1 -k	A_1 -b	A_2 -k	A_2 -b	A_3 -k	A_3 -b
(Mg_{1-x}Fe_x)(Si_{1-x}Fe_x)O₃ Pv								
V_p	9.02E-06	1.99E-06	-1.43E-03	-3.58E-04	-1.02E-02	1.96E-02	-2.785	11.869
V_s	2.81E-07	2.01E-06	-4.80E-04	-3.81E-04	6.50E-03	4.60E-03	-3.963	7.132
V_b	1.27E-05	6.76E-07	-1.57E-03	-1.07E-04	-2.44E-02	2.09E-02	0.551	8.630
(Mg_{1-x}Fe_x)(Si_{1-x}Al_x)O₃ Pv								
V_p	4.67E-06	1.58E-06	-1.64E-03	-3.26E-04	1.79E-03	2.01E-02	-0.833	11.857
V_s	-3.66E-06	1.56E-06	-6.59E-04	-3.44E-04	1.67E-02	5.24E-03	-2.130	7.091
V_b	7.05E-06	5.55E-07	-1.30E-03	-1.01E-04	-1.03E-02	2.09E-02	0.578	8.647
(Mg_{1-x}Fe_x)(Si_{1-x}Fe_x)O₃ pPv								
V_p	-4.31E-06	1.13E-06	-4.54E-04	-2.67E-04	1.29E-02	2.07E-02	-4.225	11.867
V_s	5.03E-06	4.49E-07	-1.28E-03	-2.11E-04	-2.23E-02	9.53E-03	0.097	6.833
V_b	-8.47E-06	8.94E-07	2.84E-04	-1.25E-04	3.09E-02	1.80E-02	-4.531	8.835
(Mg_{1-x}Fe_x)(Si_{1-x}Al_x)O₃ pPv								
V_p	1.62E-06	1.25E-06	-6.04E-04	-2.89E-04	2.88E-04	2.02E-02	-1.634	11.928
V_s	5.28E-06	5.39E-07	-1.18E-03	-2.20E-04	7.98E-04	8.93E-03	-1.132	6.891
V_b	-3.70E-06	1.10E-06	3.70E-04	-1.61E-04	1.84E-03	1.76E-02	-1.168	8.892

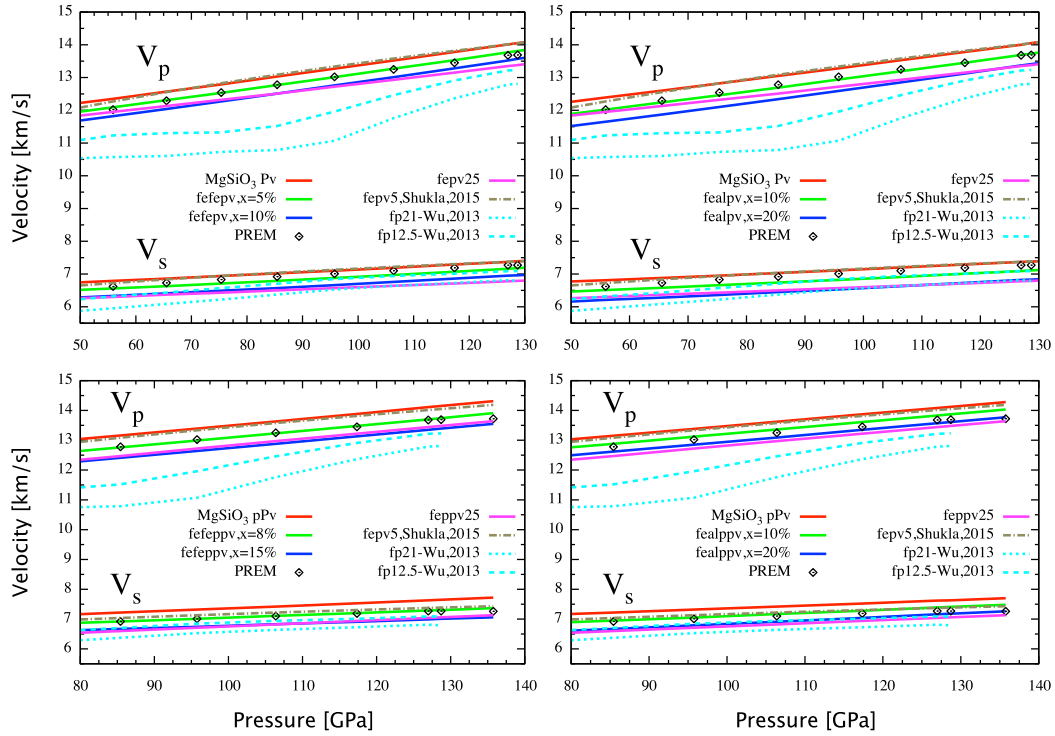


Fig. 3 (color online). The sound velocities of pure and Fe^{3+} - Fe^{3+} (fefe, left) or Fe^{3+} - Al^{3+} (feal, right) bearing MgSiO_3 in the Pv (top) and pPv (bottom) phases in comparison with that of $\text{Mg}_{0.75}\text{Fe}_{0.25}\text{SiO}_3$ (fepv25 and feppv25), $\text{Mg}_{0.95}\text{Fe}_{0.05}\text{SiO}_3$ [fepv5, from Shukla et al. (2015)], ferropericlase [fp21 and fp12.5, from Wu et al. (2013)], and the PREM along the geotherm by Brown and Shankland (1981).

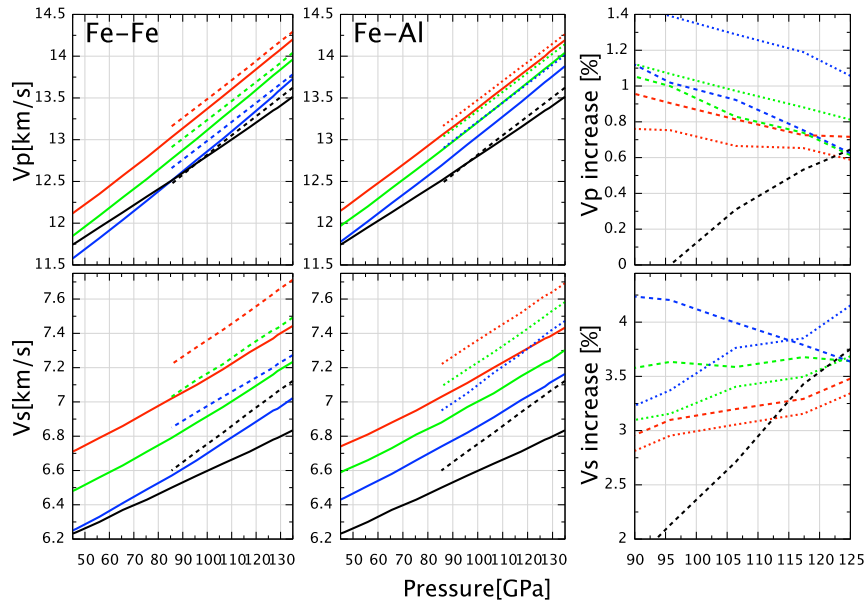


Fig. 4 (color online). The sound velocities of Fe^{3+} - Fe^{3+} (Fe-Fe, left) or Fe^{3+} - Al^{3+} (Fe-Al, center) bearing MgSiO_3 Pv (solid curves) and pPv (dashed or dotted curves) with $x=0.0$ (red) $x=5\%$ (green) and $x=10\%$ (blue). The corresponding velocities increases from Pv to pPv phases are shown in the right panel. Corresponding results for $\text{Mg}_{0.75}\text{Fe}_{0.25}\text{SiO}_3$ are also plotted (black curves) for comparison.

We investigate the relation between density and P , T and x by starting from the Vinet equation of state (EoS). The EoS has three ambient parameters, ρ_0 , K_0 , and K_0' , and is an isothermal equation that has been widely used for minerals at Earth-interior conditions. Here, we assume linear dependence of ρ_0 and K_0 , and independence of K_0' , on T , and fit P as a function of ρ and T for each iron or aluminum content x . Finally, we fit the density at each P , T condition linearly to x , for systems with Fe^{2+} , Fe^{3+} - Fe^{3+} , and Fe^{3+} - Al^{3+} , respectively. We plot density along a geotherm (Brown and Shankland, 1981) and compare with ferropericlase and the preliminary reference Earth model (PREM) (Dziewonski and Anderson, 1981), as shown in Fig. 5. Our results show that (Fig. 6), at 110 GPa, the density of the pPv phase is higher than that of Pv by about 1.5% when Fe or Al presents, similar to that in pure MgSiO_3 . The density difference between Pv and pPv decreases with the Fe^{3+} - Al^{3+} concentration, opposite to the trends in velocities differences; whereas it is less sensitive to Fe^{3+} - Fe^{3+} than to Fe^{3+} - Al^{3+} , similar to that in velocities.

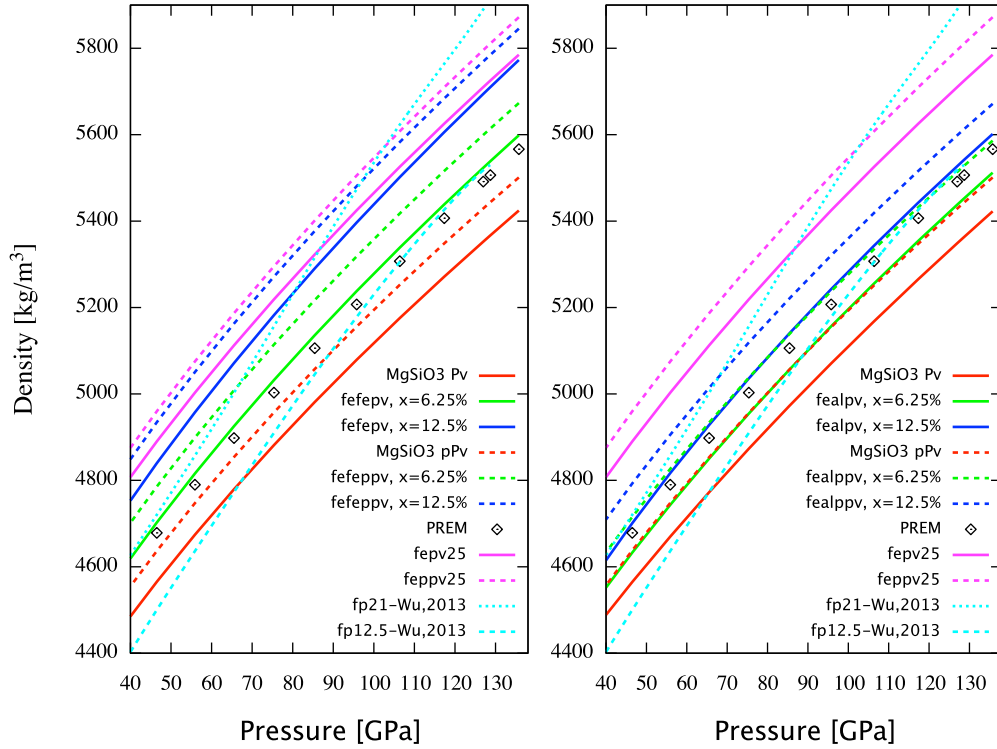


Fig. 5 (color online). The density profile of pure and Fe^{3+} - Fe^{3+} (fefe, left) or Fe^{3+} - Al^{3+} (feal, right) bearing MgSiO_3 in the Pv and pPv phases, in comparison with that of $\text{Mg}_{0.75}\text{Fe}_{0.25}\text{SiO}_3$ (fepv25 and feppv25), ferropericlasite [fp21 or fp12.5, from Wu et al. (2013)] and PREM along the geotherm (Brown and Shankland, 1981).

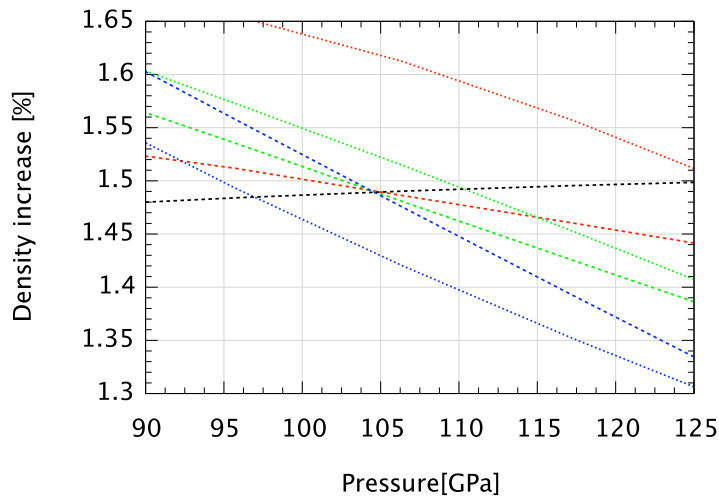


Fig. 6 (color online). The density increase from Pv to pPv phases for Fe^{3+} - Fe^{3+} (dashed curves) or Fe^{3+} - Al^{3+} (dotted curves) bearing MgSiO_3 with $x=0.0$ (red) $x=6.25\%$ (green) and $x=12.5\%$ (blue). Corresponding results for $\text{Mg}_{0.75}\text{Fe}_{0.25}\text{SiO}_3$ are also plotted (dash black) for comparison.

3.5. Elastic anisotropy

The shear wave anisotropy $AV_S = \left| \frac{V_{S1} - V_{S2}}{(V_{S1} + V_{S2})/2} \right|$ of Fe/Al-bearing Pv and pPv are studied as functions of P and T (Walker and Wookey, 2012) for waves traveling along the three axes. As expected from the structural differences between Pv and pPv, we found much higher AV_S in pPv than Pv (~10-30% vs ~10%). In Pv, shear waves travelling along [001] are slightly more anisotropic than those along [100] and [010], while in pPv it is the opposite. The dependence of anisotropy on P and T is weak in general, potentially explained by the stability of the structures with compression or heating in lower-mantle conditions. Our results (Figs. S7-8) also suggest that the inclusion of Fe or Al increases the anisotropy of MgSiO₃ pPv but this is not the case for Pv.

4. Geophysical implications

4.1. Mineralogical composition of the lower mantle

The above calculations enable us to consider mineral assemblages and evaluate their density and sound velocities. By comparing these results with a seismic velocity model, such as the PREM, one can propose a mineralogical composition for the lower mantle, which is important for understanding the formation and evolution of the Earth and other planets, but impossible to directly determine.

To achieve this, we first examine a mixture of Mg_{0.95}Fe_{0.05}SiO₃:Mg_{1-x}Fe_xSi_{1-x}Fe_xO₃:Mg_{1-x}Fe_xSi_{1-x}Al_xO₃:Fe_{0.125}Mg_{0.875}O=34:10:43:13 (volume ratio), which corresponds to a mole ratio perovskite:ferropericlasite=75:25, close to the pyrolitic composition that was proposed for the upper mantle, but is also widely assumed for the lower mantle. Here, the moduli and density values for Mg_{0.95}Fe_{0.05}SiO₃ and Fe_{0.125}Mg_{0.875}O are based on Shukla et al. (2015) and Wu et al. (2013), respectively. Our calculation shows that, when choosing $x=0.06$ in Mg_{1-x}Fe_xSi_{1-x}Al_xO₃ and $x=0.05$ in Mg_{1-x}Fe_xSi_{1-x}Fe_xO₃, the velocities match PREM very well

from 50 GPa to the top of the D'' (Fig. 7, left), and the agreement in density is also good (difference < 1.2%).

In such an assemblage, the number of cations per 12 O is Mg: 4.48, Si: 3.45, Fe: 0.37, Al: 0.11, with Mg/Si=1.29 and Mg# = Mg/(Mg+Fe)=0.92, which are remarkably consistent with that in pyrolite (Mg/Si=1.27±0.06, Mg#=0.90±0.05, see, for example, Table 1 in Lee et al., 2004). Therefore, neglecting minor phases such as CaSiO₃, we can conclude that the major part of the Earth's mantle resembles the pyrolitic model. This is in contrast to the silicon-rich model for the Earth's lower mantle and implies that the extra silicon relative to the CI chondrite may reside in the D'' region or the core (Komabayashi et al., 2010).

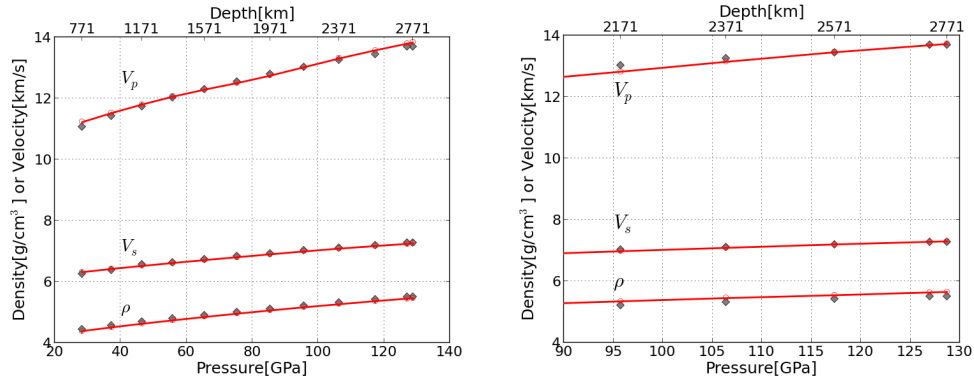


Fig. 7 (color online). Comparing density and velocities of mineral assemblages with that of PREM (black diamond points) assuming the geotherm by Brown and Shankland (1981). Left, the assemblage consists of 34 vol.% Mg_{0.95}Fe_{0.05}SiO₃, 10 vol.% Mg_{0.95}Fe_{0.05}Si_{0.95}Fe_{0.05}O₃, and 43 vol.% Mg_{0.94}Fe_{0.06}Si_{0.94}Al_{0.06}O₃ in the Pv phase and 13 vol.% Fe_{0.125}Mg_{0.875}O; right: it consists of 26 vol.% Mg_{0.95}Fe_{0.05}SiO₃, 10 vol.% Mg_{0.9}Fe_{0.1}Si_{0.9}Fe_{0.1}O₃, and 53 vol.% Mg_{0.85}Fe_{0.15}Si_{0.85}Al_{0.15}O₃ in the pPv phase and 11 vol.% Fe_{0.21}Mg_{0.79}O. Mg_{0.95}Fe_{0.05}SiO₃ data are estimated with the BurnMan code (Cottaar et al., 2014b) by applying the thermodynamic model of Stixrude and Lithgow-Bertelloni (2011) on the calculation by Shukla, et al. (2015). For the pPv phase of Mg_{0.95}Fe_{0.05}SiO₃, K^S is estimated to be the same as that of the Pv phase, G and ρ are estimated to be 5% and 1.5% larger than that of the Pv phase, respectively. Ferropericlase data are from Wu, et al. (2013).

At higher pressures when Pv can be less stable than pPv, we find that, with higher Al concentration in the pPv phase and less ferropericlase but with higher iron content, the velocities of the assemblage fit PREM values well in the high-pressure region (>105 GPa) (Fig. 7, right), although the density ρ is slightly higher (by 2.6%). If such an assemblage exists, the per 12 O cation numbers (Mg: 4.06, Si: 3.28, Fe: 0.68, Al: 0.33) indicate lower

Mg/Si ratio (1.23) and Mg# (0.86), which still agree with that in pyrolite, but more Fe (Fe^{2+} and Fe^{3+} totals) and Al^{3+} than the major part of the mantle above. The increase in ferric iron ($\text{Fe}^{3+}/\Sigma\text{Fe}$ from 0.39 to 0.60) can be partially explained by the $\text{Fe}^{2+} \rightarrow \text{Fe}^{3+}$ transformation driven by charge disproportionation, considering the low oxygen fugacity of the lower mantle (Xu et al., 2015), and may as well outstand the role of Al^{3+} in the silicates. However, there are shortcomings to this approach in the D''. First, the Brown and Shankland geotherm that we are using here neglects the steep thermal gradient expected near the core-mantle boundary (CMB). In the lowermost few hundred kilometers, the temperature could be underestimated by a few hundred to 1500 K, which in turn means that the velocities and the density of the mineral assemblage are overestimated (by about 1% for V_p , 2% V_s , and 1% for ρ). Including the temperature effects could support an assemblage with similar composition (perovskite:ferropericlae mole ratio 74:26, Mg#=0.90, Mg/Si=1.26, $\text{Fe}^{3+}/\Sigma\text{Fe}$ =0.31) to the major part of the lower mantle above but more iron-enriched in ferropericlae (Fig. 8), which currently overestimates V_p , V_s , and ρ by 1.0%, 1.7%, and 1.3%, respectively, in the pPv region. Second, the Voigt averaging scheme for pPv is also associated by an uncertainty of ~1% for V_p and V_s (see supplementary Table S5). Lastly, both velocity and density variations are significant in the lowermost mantle and could reflect significant thermal and compositional variations (see supplementary material).

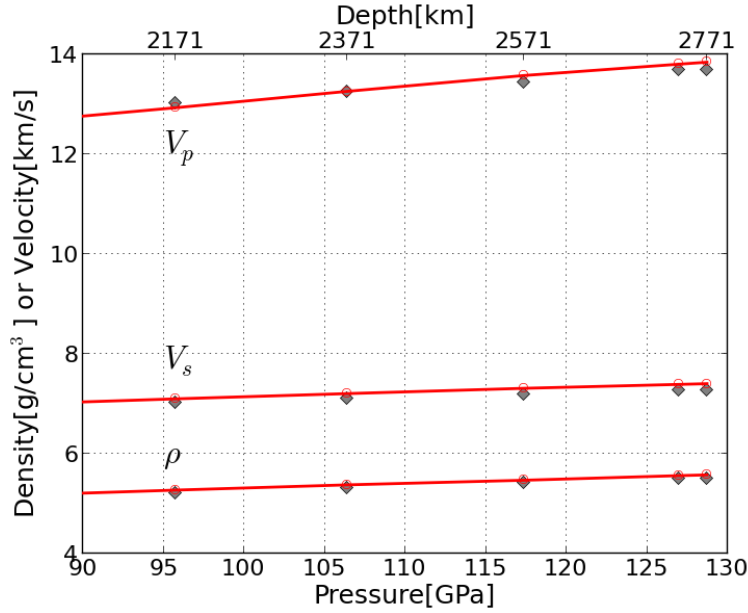


Fig. 8 (color online). The velocities and density of an assemblage consisting of 34 vol.% $\text{Mg}_{0.95}\text{Fe}_{0.05}\text{SiO}_3$, 10 vol.% $\text{Mg}_{0.95}\text{Fe}_{0.05}\text{Si}_{0.95}\text{Fe}_{0.05}\text{O}_3$, and 43 vol.% $\text{Mg}_{0.94}\text{Fe}_{0.06}\text{Si}_{0.94}\text{Al}_{0.06}\text{O}_3$ in the pPv phase and 13 vol.% $\text{Fe}_{0.21}\text{Mg}_{0.79}\text{O}$ in comparison with that of PREM (black diamond points) assuming the geotherm by Brown and Shankland (1981). $\text{Mg}_{0.95}\text{Fe}_{0.05}\text{SiO}_3$ and ferropericlase data are obtained in the same way as that in Fig. 7.

4.2. Seismic anisotropy

While the lower mantle is thought to be mostly isotropic, seismic anisotropy is observed in D". The main characteristic is that horizontally polarized waves travel faster than vertically polarized ones (or $\xi = V_{\text{SH}}^2 / V_{\text{SV}}^2 > 1$) in regions beneath subducting slabs in regional studies as well as in global models. Observations of seismic anisotropy in D" are often explained by crystal preferred orientation in post-perovskite (Cottaar et al. 2014a), but these studies have so far ignored major element composition. Based on the elastic constants in this study, we forward model the resulting texture and seismic anisotropy in perovskite and post-perovskite using the Viscoplastic Self-Consistent (VPSC) method (Lebensohn and Tomé, 1993) and deformation information from a typical tracer within a subducting slab (Cottaar et al., 2014a). While many slip systems are active within the model, we denote different experiments by the slip plane of their most active slip system. For perovskite this is (001), while for post-perovskite this is either (100), (010) or (001) (Cottaar et al.,

2014a). For the perovskite model with dominant (001) slip we see an incompatible signature of $\xi < 1$ across all compositions, pressures and temperatures, and we do not show these results here.

The resulting shear wave splitting and ξ values for post-perovskite are shown in Fig. 9 at 100 GPa and 2500 K. Overall, we see that the transverse isotropy scales with the strength and orientation of splitting in the horizontal plane. The (100) and (001) cases show consistent signs in ξ with major element composition: (100) produces a signature opposite from the one seen in seismology, while (001) is consistent with seismology. The resulting ξ for the (010) case on the other hand is close to 1 and varies in amplitude; ξ increases for $x=8\%$ compared to $x=0\%$, but loses all amplitude when $x=17\%$. Regardless of this trend, the amplitudes of ξ for the (010) case are too weak to explain seismic observations. Generally, seismic observations will underestimate the actual amplitudes at depth, while our modeling will overestimate the amplitudes due to assuming pure dislocation creep as the deformation mechanism and by excluding the presence of periclase. This leaves the (001) case as the only compatible mechanism for seismic transverse isotropy, insensitive to the amount of Fe or Al included. None of the models predict strong azimuthal anisotropy, i.e. splitting through the vertical axis.

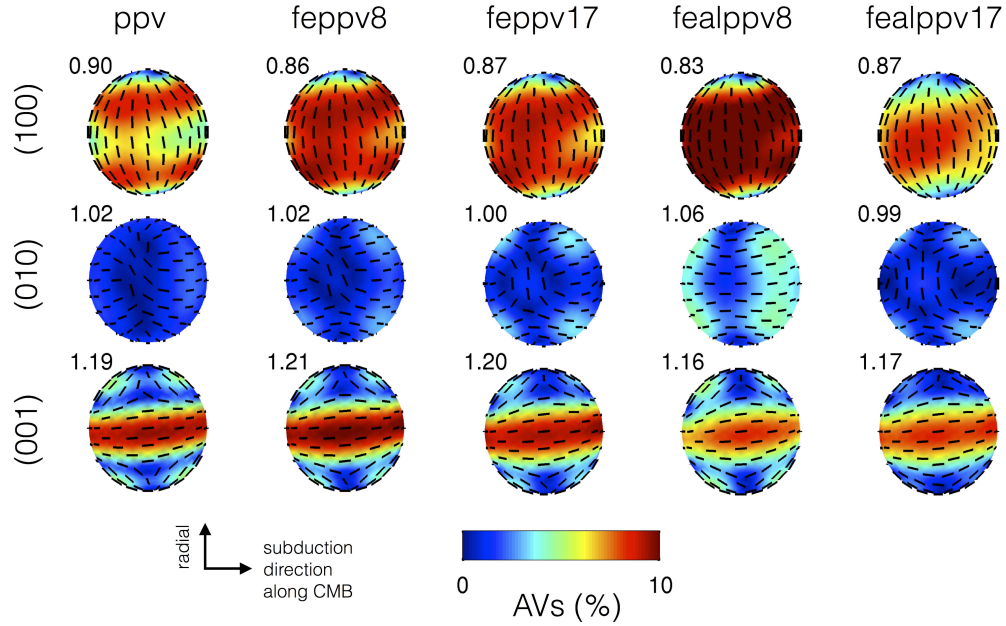


Fig. 9 (color online). Shear wave splitting strength (AVs, in color) and fast axis direction (black bar) shown as a function of seismic wave propagation direction on a sphere for the five different compositional model and three different sets of slips systems. The horizontal plane is parallel to the CMB with the direction of subduction to the right. The value for transverse isotropy, $\xi = V_{SH}^2/V_{SV}^2$, is given in the upper left corner of each subplot. Figure is made with Matlab Seismic Anisotropy Toolkit (Walker and Wookey, 2012) ppv: pure $MgSiO_3$ pPv; feppv8 or feppv17: Fe^{3+} - Fe^{3+} bearing $MgSiO_3$ with $x=8\%$ or 17% ; fealppv8 or fealppv17: Fe^{3+} - Al^{3+} bearing $MgSiO_3$ with $x=8\%$ or 17% .

5. Conclusion

The thermoelasticity of pure, as well as Fe- and Al-bearing $MgSiO_3$ bridgmanite and post-perovskite have been calculated at a variety of P , T conditions and Fe or Al compositions. Our results show that the presence of Fe, especially Fe^{3+} , and Al results in complicated characteristics in the elastic and seismic properties of these minerals, depending on the their content and distribution, the phase of the mineral, and the P , T conditions. Our results, when combined with values previously calculated for (Fe,Mg)O, allow us to calculate the seismic properties of mineral assemblages and thus explore the probable composition of the lower mantle. We show that the average lower mantle seismic velocities and density can be fit with a pyrolitic composition. We also study the transverse anisotropy of these minerals in a subducting slab near the CMB, and confirm that the pPv phase with predominant (001) slip plane matches the seismic anisotropy in the D'' region

independent of the amount of Fe or Al. These results provide a useful resource that can be used to investigate the effect of impurities on the properties of mineral assemblages in the deep mantle.

Acknowledgement

Computational resources for this work were mainly provided by NSF-MRI Grant CNS-0821794, MRI-Consortium: Acquisition of a Supercomputer by the Front Range Computing Consortium (FRCC), with additional support from the University of Colorado and NSF sponsorship of the National Center for Atmospheric Research. Additional computational resources were provided by the National Energy Research Scientific Computing Center, a DOE Office of Science User Facility supported by the Office of Science of the U.S. Department of Energy under Contract No. DE-AC02-05CH11231. We also acknowledge the use of high performance computing provided by Advanced Research Computing at the University of Leeds. The authors appreciate Ian Rose, Rudy Wenk, Raymond Jeanloz, B. K. Godwal and Barbara Romanowicz for discussion and thank Mingming Li and Allen McNamara for providing the deformation information within a subducting slab. S. Zhang and B. Militzer acknowledge the support from NSF and the grant EAR/CSEDI 1067513. S. Stackhouse and T. Liu were supported, in part, by NERC grant number NE/K006290/1. S. Cottaar is funded by the Drapers' Company Research Fellowship from Pembroke College, Cambridge, UK. Critical and constructive comments from two anonymous reviewers as well as Editor Peter Shearer are highly appreciated.

Appendix A. Supplementary material

Supplementary material related to this article has been attached.

References

- Badro, J., Rueff, J.-P., Vankó, G., Monaco, G., Fiquet, G., Guyot, F., 2004. Electronic transitions in perovskite: possible nonconvecting layers in the lower mantle. *Science* 305 (5682), 383–386. doi:10.1126/science.1098840
- Brown, J.M., Shankland, T.J., 1981. Thermodynamic parameters in the Earth as determined from seismic profiles. *Geophys. J. R. Astr. Soc.* 66, 579–596.
- Brodholt, J., 2000. Pressure-induced changes in the compression mechanism of aluminous perovskite in the Earth's mantle. *Nature* 407 (6804), 620–622. doi:10.1038/35036565
- Caracas, R., Cohen, R.E., 2005. Effect of chemistry on the stability and elasticity of the perovskite and post-perovskite phases in the MgSiO_3 - FeSiO_3 - Al_2O_3 system and implications for the lowermost mantle. *Geophys. Res. Lett.* 32 (16), L16310. doi:10.1029/2005GL023164
- Catalli, K., Shim, S.-H., Dera, P., Prakapenka, V.B., Zhao, J., Sturhahn, W., Chow, P., Xiao, Y., Cynn, H., Evans, W.J., 2011. Effects of the Fe^{3+} spin transition on the properties of aluminous perovskite—New insights for lower-mantle seismic heterogeneities. *Earth Planet. Sci. Lett.* 310 (3-4), 293–302. doi:10.1016/j.epsl.2011.08.018
- Ceperley, D.M., Alder, B.J., 1980. Ground State of the Electron Gas by a Stochastic Method. *Phys. Rev. Lett.* 45, 566. <http://dx.doi.org/10.1103/PhysRevLett.45.566>
- Cottaar, S., Li, M., McNamara, A.K., Romanowicz, B., Wenk, H.-R., 2014a. Synthetic seismic anisotropy models within a slab impinging on the core-mantle boundary. *Geophys. J. Int.* 199 (1), 164–177. doi:10.1093/gji/ggu244
- Cottaar, S., Heister, T., Rose, I., Unterborn, C., 2014b. BurnMan: A lower mantle mineral physics toolkit, *Geochem. Geophys. Geosyst.* 15, 1164–1179.
- Dziewonski, A.M., Anderson, D.L., 1981. Preliminary reference Earth model. *Phys. Earth Planet. Inter.* 25 (4), 297–356. doi:10.1016/0031-9201(81)90046-7
- Fujino, K., Nishio-Hamane, D., Nagai, T., Seto, Y., Kuwayama, Y., Whitaker, M., Ohfuji, H., Shinmei, T., Irifune, T., 2014. Spin transition, substitution, and partitioning of iron in lower mantle minerals. *Phys. Earth Planet. Inter.* 228, 186–191. doi:10.1016/j.pepi.2013.12.008
- Hsu, H., Umemoto, K., Cococcioni, M., Wentzcovitch, R.M., 2011a. The Hubbard U correction for iron-bearing minerals: A discussion based on $(\text{Mg,Fe})\text{SiO}_3$ perovskite. *Phys. Earth. Planet. Inter.* 185, 13–19. doi:10.1016/j.pepi.2010.12.001
- Hsu, H., Blaha, P., Cococcioni, M., Wentzcovitch, R., 2011b. Spin-State Crossover and Hyperfine Interactions of Ferric Iron in MgSiO_3 Perovskite. *Phys. Rev. Lett.* 106 (11), 118501. doi:10.1103/PhysRevLett.106.118501
- Hsu, H., Yu, Y.G., Wentzcovitch, R.M., 2012. Spin crossover of iron in aluminous MgSiO_3 perovskite and post-perovskite. *Earth Planet. Sci. Lett.* 359–360, 34–39. doi:10.1016/j.epsl.2012.09.029

- Irifune, T., Shinmei, T., McCammon, C.A., Miyajima, N., Rubie, D.C., Frost, D.J., 2010. Iron partitioning and density changes of pyrolite in Earth's lower mantle. *Science* 327 (5962), 193–5. doi:10.1126/science.1181443
- Kiefer, B., Stixrude, L., Wentzcovitch, R.M., 2002. Elasticity of (Mg, Fe) SiO₃ -Perovskite at high pressures. *Geophys. Res. Lett.* 29 (11), 34.
- Komabayashi, T., Hirose, K., Nagaya, Y., Sugimura, E., Ohishi, Y., 2010. High-temperature compression of ferropericlase and the effect of temperature on iron spin transition. *Earth Planet. Sci. Lett.* 297, 691. doi:10.1016/j.epsl.2010.07.025
- Kresse, G., Furthmüller, J., 1996. Efficient iterative schemes for ab initio total-energy calculations using a plane-wave basis set. *Phys. Rev. B* 54, 11169. <http://dx.doi.org/10.1103/PhysRevB.54.11169>
- Lebensohn, R., Tomé, C., 1993. A self-consistent anisotropic approach for the simulation of plastic deformation and texture development of polycrystals: application to zirconium alloys. *Acta Met. Mater.* 41, 2611–2624, doi:10.1016/0956-7151(93)90130-K
- Lee, K. K. M., O'Neill, B., Panero, W.R., Shim, S.H., Benedetti, L.R., Jeanloz, R., 2004. Equations of state of the high-pressure phases of a natural peridotite and implications for the Earth's lower mantle. *Earth Planet. Sci. Lett.* 223 (3-4), 381–393. doi:10.1016/j.epsl.2004.04.033
- Li, L., Brodholt, J.P., Stackhouse, S., Weidner, D.J., Alfredsson, M., Price, G.D., 2005a. Elasticity of (Mg,Fe)(Si,Al)O₃ perovskite at high pressure. *Earth Planet. Sci. Lett.* 240, 529-536. doi:10.1016/j.epsl.2005.09.030
- Li, L., Brodholt, J.P., Stackhouse, S., Weidner, D.J., Alfredsson, M., Price, G.D., 2005b. Electronic spin state of ferric iron in Al-bearing perovskite in the lower mantle. *Geophys. Res. Lett.* 32 (17), L17307. doi:10.1029/2005GL023045
- Mao, W.L., Shen, G., Prakapenka, V.B., Meng, Y., Campbell, A.J., Heinz, D.L., Shu, J., Hemley, R.J., Mao, H., 2004. Ferromagnesian postperovskite silicates in the D'' layer of the Earth. *Proc. Natl. Acad. Sci. USA* 101 (45), 15867–15869.
- Metsue, A., Tsuchiya, T., 2011. Lattice dynamics and thermodynamic properties of (Mg,Fe₂₊)SiO₃ postperovskite. *J. Geophys. Res.* 116 (B8), 1–11. doi:10.1029/2010JB008018
- Militzer, B., Wenk, H.-R., Stackhouse, S., Stixrude, L., 2011. First-principles calculation of the elastic moduli of sheet silicates and their application to shale anisotropy. *Am. Mineral.* 96 (1), 125–137. doi:10.2138/am.2011.3558
- Muir, J.M.R., Brodholt, J.P., 2015. Elastic properties of ferrous bearing MgSiO₃ and their relevance to ULVZs. *Geophys. J. Int.* 201 (1), 496–504. doi:10.1093/gji/ggv045
- Murakami, M., Ohishi, Y., Hirao, N., Hirose, K., 2012. A perovskitic lower mantle inferred from high-pressure, high-temperature sound velocity data. *Nature* 485 (7396), 90–4. doi:10.1038/nature11004
- Nosé, S., 1984. A unified formulation of the constant temperature molecular-dynamics methods. *J. Chem. Phys.* 81 (1): 511–519. doi:10.1063/1.447334
- Oganov, A.R., Brodholt, J.P., Price, G.D., 2001. Ab initio elasticity and thermal equation of state of MgSiO₃ perovskite. *Earth Planet. Sci. Lett.* 184, 555-560

- Oganov, A.R., Ono, S., 2004. Theoretical and experimental evidence for a post-perovskite phase of MgSiO₃ in Earth's D" layer. *Nature* 430 (6998), 445–8. doi:10.1038/nature02701
- Shukla, G., Wu, Z., Hsu, H., Floris, A., Cococcioni, M., Wentzcovitch, R.M., 2015. Thermoelasticity of Fe²⁺-bearing bridgmanite, *Geophys. Res. Lett.* 42, doi:10.1002/2014GL062888
- Shim, S.-H., 2008. The Postperovskite Transition. *Annu. Rev. Earth Planet. Sci.* 36 (1), 569–599. doi:10.1146/annurev.earth.36.031207.124309
- Stackhouse, S., Brodholt, J.P., Wookey, J., Kendall, J.-M., Price, G.D., 2005. The effect of temperature on the seismic anisotropy of the perovskite and post-perovskite polymorphs of MgSiO₃. *Earth Planet. Sci. Lett.* 230 (1-2), 1–10. doi:10.1016/j.epsl.2004.11.021
- Stackhouse, S., Brodholt, J.P., Dobson, D.P., Price, G.D., 2006. Electronic spin transitions and the seismic properties of ferrous iron-bearing MgSiO₃ post-perovskite. *Geophys. Res. Lett.* 33 (12), L12S03. doi:10.1029/2005GL025589
- Stackhouse, S., Brodholt, J.P., Price, G. D., 2007. Electronic spin transitions in iron-bearing MgSiO₃ perovskite. *Earth Planet. Sci. Lett.* 253 (1-2), 282–290. doi:10.1016/j.epsl.2006.10.035
- Stackhouse, S., Brodholt, J.P., 2007. The High-Temperature Elasticity of MgSiO₃ Post-Perovskite. In *Post-Perovskite: The Last Mantle Phase Transition* (pp. 99–113).
- Stackhouse, S., Stixrude L.P., Karki, B.B., 2010. Determination of the high-pressure properties of fayalite from first-principles. *Earth Planet. Sci. Lett.* 289 (1-2), 449–456. doi:10.1016/j.epsl.2009.11.033
- Stixrude, L., Lithgow-Bertelloni, C., 2011. Thermodynamics of mantle minerals – II. Phase equilibria. *Geophys. J. Int.* 184, 1180–1213.
- Tsuchiya, T., Tsuchiya, J., Umemoto, K., Wentzcovitch, R.M., 2004. Phase transition in MgSiO₃ perovskite in the earth's lower mantle. *Earth Planet. Sci. Lett.* 224 (3-4), 241–248. doi:10.1016/j.epsl.2004.05.017
- Tsuchiya, T., Tsuchiya, J., 2006. Effect of impurity on the elasticity of perovskite and postperovskite: Velocity contrast across the postperovskite transition in (Mg,Fe,Al)(Si,Al)O₃. *Geophys. Res. Lett.* 33 (12), L12S04. doi:10.1029/2006GL025706
- Tsuchiya, T., Wang, X., 2013. Ab initio investigation on the high-temperature thermodynamic properties of Fe³⁺-bearing MgSiO₃ perovskite. *J. Geophys. Res.* 118 (1), 83–91. doi:10.1029/2012JB009696
- Wallace, D., 1972. *Thermodynamics of Crystals*. Wiley, New York.
- Walker, A. M., Wookey, J., 2012. MSAT-A new toolkit for the analysis of elastic and seismic anisotropy. *Compu. Geosci.* 49, 81–90. doi:10.1016/j.cageo.2012.05.031
- Wentzcovitch, R., Karki, B., Cococcioni, M., de Gironcoli, S., 2004. Thermoelastic Properties of MgSiO₃-Perovskite: Insights on the Nature of the Earth's Lower Mantle. *Phys. Rev. Lett.* 92 (1), 018501. doi:10.1103/PhysRevLett.92.018501
- Wentzcovitch, R.M., Tsuchiya, T., Tsuchiya, J., 2006. MgSiO₃ postperovskite at D" conditions. *Proc. Natl. Acad. Sci. USA* 103 (3), 543–6. doi:10.1073/pnas.0506879103

- Wu, Z., Justo, J. F., Wentzcovitch, R.M., 2013. Elastic Anomalies in a Spin-Crossover System: Ferropericlaase at Lower Mantle Conditions. *Phys. Rev. Lett.* 110 (22), 228501. doi:10.1103/PhysRevLett.110.228501
- Xu, S., Shim, S., Morgan, D., 2015. Origin of Fe³⁺ in Fe-containing , Al-free mantle silicate perovskite. *Earth Planet. Sci. Lett.* 409, 319–328.
- Yu, Y.G., Hsu, H., Cococcioni, M., Wentzcovitch, R.M., 2012. Spin states and hyperfine interactions of iron incorporates in MgSiO₃ post-perovskite. *Earth Planet. Sci. Lett.* 331-332, 1–7. doi:10.1016/j.epsl.2012.03.002
- Zhang, F., Oganov, A.R., 2006a. Mechanisms of Al³⁺ incorporation in MgSiO₃ post-perovskite at high pressures. *Earth Planet. Sci. Lett.* 248 (1-2), 69–76. doi:10.1016/j.epsl.2006.05.015
- Zhang, F., Oganov, A.R., 2006b. Valence state and spin transitions of iron in Earth’s mantle silicates. *Earth Planet. Sci. Lett.* 249 (3-4), 436–443. doi:10.1016/j.epsl.2006.07.023
- Zhang, Z., Stixrude, L., Brodholt, J., 2013. Elastic properties of MgSiO₃-perovskite under lower mantle conditions and the composition of the deep Earth. *Earth Planet. Sci. Lett.* 379, 1–12. doi:10.1016/j.epsl.2013.07.034